energy&fuels

Article

pubs.acs.org/EF

Reactive Transport Modeling of Interactions between Acid Gas (CO_2 + H_2S) and Pozzolan-Amended Wellbore Cement under Geologic Carbon Sequestration Conditions

Liwei Zhang,*[,†] David A. Dzombak,[†] David V. Nakles,[†] Jean-Patrick Leopold Brunet,[‡] and Li Li[‡]

[†]Department of Civil and Environmental Engineering, Carnegie Mellon University, Pittsburgh, Pennsylvania, 15213-3890, United States

[‡]Department of Energy and Mineral Engineering, Pennsylvania State University, University Park, Pennsylvania, 16802, United States

Supporting Information

ABSTRACT: The implementation of acid gas cosequestration requires investigation of the potential for acid gas leakage along existing wellbores at sequestration sites. In this study, the interaction between pozzolan-amended wellbore cement (35 vol % pozzolan/65 vol % cement, hereafter referred to as 35:65 sample) and acid gas (e.g., a mixture of CO_2 and H_2S) was simulated using the reactive transport code CrunchFlow. The model was applied to describe, interpret, and extrapolate scanning electron microscopy-backscattered electron (SEM-BSE) and scanning electron microscopy-energy dispersive spectroscopy (SEM-EDS) results on pozzolan-amended cement samples exposed to a 1 wt % NaCl solution saturated with an acid gas mixture of 21 mol % H_2S and 79 mol % CO_2 under the temperature of 50 °C and pressure of 150 bar. Simulation outputs included calcite volume percentage, total Ca and S weight percentages in the solid phase, porosity, and effective permeability from the surface to the interior of pozzolan-amended wellbore cement. The model reproduced the observed calcite zone formed in the brine-cement interface region of the sample after 2.5 days of exposure. The model also predicted that the calcite layer became dense (calcite vol % in the layer reached 55%) after 90 days of exposure, consistent with the experimental observation. C−S−H was the primary Ca^{2+} source to form the calcite layer, followed by C3S and $Ca(OH)_2$. The main observed products of reaction between the 35:65 sample and H_2S were pyrite and ettringite. Pyrite was primarily formed within 0.5 mm from the brine-cement interface; ettringite mainly formed within 1 mm from the interface. The model simulated these reactions that only the interface region (up to 2 mm distance from the surface) of the 35:65 sample became porous after 30 years of exposure. However, this narrow porous region could still serve as a migration pathway for acid gas, which was indicated by the increase in effective parallel permeability values determined from the simulation results. Those results show consistency with results of neat cement samples exposed under similar conditions. An increase in H_2S content (in the range of 0 mol % to 40 mol %) results in more dissolution of Ca-bearing minerals in cement and more precipitation of calcite. Overall, this study indicates that an increase of porosity and permeability of pozzolan-amended wellbore cement at the cement interface with brine saturated with CO_2 and H_2S can cause significant changes in effective permeability of the cement.

1. INTRODUCTION

CO_2 concentration in the atmosphere has increased significantly since the advent of the industrial age.[1,2] A correlation between atmospheric CO_2 concentration increase and global temperature increase is supported by many studies.[3,4] An important strategy to help reduce the atmospheric CO_2 concentration is to capture CO_2 from large point sources such as electric power plants and store the captured CO_2 in natural or human-made carbon sinks.[2] Because some industrial processes (e.g., purification of sour natural gas and precombustion of coal) simultaneously release CO_2 and H_2S (hereafter referred to as "acid gas"), capture and sequestration of acid gas have also been studied.[5−8] The H_2S content in flue gases from coal combustion is typically less than 10% (captured without gas separation), but the H_2S content in acid gas separated from sour natural gas can reach as high as 85%.[9]

One of the major public concerns about carbon capture and sequestration, especially the sequestration of acid gas, is the risk of leakage from the storage site.[10−12] Leakage of injected gas can potentially cause water acidification and leads to the deterioration of water quality due to multiple reactions.[13−16] Abandoned wellbores are a potentially important leakage pathway for CO_2 and H_2S to escape from the storage site,[2,17] because acid gas can react with wellbore cement and cause cement integrity degradation. The reactions can potentially create several possible leakage pathways along a well, especially at the caprock−cement interface and the casing−cement interface.[2] A methodology to evaluate the alteration of wellbore cement by CO_2/H_2S in geologic acid gas cosequestration conditions is needed.

Although studies on cement−CO_2 interactions have been extensive, there have been only a few experimental studies focused on wellbore cement alteration induced by acid gas attack in geologic carbon sequestration conditions.[7,8] Kutchko et al. observed that neat cement exposed to a mixture of CO_2 and H_2S exhibited a carbonated zone similar to the samples exposed to

Received: August 30, 2013
Revised: October 22, 2013
Published: October 24, 2013

 © 2013 American Chemical Society dx.doi.org/10.1021/ef401749x | Energy Fuels 2013, 27, 6921−6937

CO_2 only, and pyrite and ettringite were formed in the rim region and the core region of the sample, respectively.[7] Jacquemet et al. observed that there was a fast formation of a nonporous calcite coating on the cement surface, which effectively blocked the diffusion of both CO_2 and H_2S to the interior region of the cement.[8] Zhang et al. observed that the degree of pozzolan-amended cement alteration induced by acid gas attack depended on pozzolan content. The pozzolan-amended cement with 35 vol % pozzolan additives was altered only in the region close to the surface after 90 days of exposure to acid gas, while the pozzolan-amended cement with 65 vol % pozzolan additive was altered in both the surface and interior regions after 2.5 days of exposure to acid gas.[18] The alteration rates of pozzolan-amended cement with 35 vol % pozzolan additive exposed to acid gas were also quantified by authors of this paper. The CO_2 alteration rate was 3.3×10^{-3} mm/day, and the H_2S alteration rate was 4.3×10^{-3} mm/day. Pozzolan is added to reduce the density of the slurry and reduce the amount of cement needed, which means a reduction of cost. Pozzolan rich in silica fume can also significantly contribute to the compressive strength development of oil well cement.[19] As the addition of pozzolan helps combat strength retrogression (which would occur at the high temperatures encountered in deeper oil wells),[20] pozzolan-amended wellbore cement has been widely used in oil well construction, and American Petroleum Institute (API) specified standard procedures to prepare pozzolan-amended wellbore cement in 1991.[21]

While experimental studies have enabled insights into the reaction pathways of wellbore cement−acid gas interaction, such studies have limitations. First, they are limited to relatively short time scales. Predicting the long-term interactions (e.g., 30−100 years) between the wellbore cement and acid gas is very important under conditions relevant to carbon sequestration. Second, sensitivity analyses on controlling variables, including effects of H_2S concentration on cement−acid gas interaction, are time-consuming and expensive.

Computer-based reactive transport modeling overcomes these limitations, enabling extrapolation of experimental findings to longer time scales and parameter sensitivity analyses. Reactive transport models can be used to (1) predict the changes in physical and chemical properties of wellbore cement after long exposure times (e.g., 30 years), which cannot be obtained from experimental data; (2) predict porosity and permeability changes from the surface to the interior of the cement; (3) conduct sensitivity analyses via simulation, for example, to study how changes in H_2S concentration can affect physical and chemical properties of wellbore cement.

The main objective of this study was to develop a reactive transport model to investigate quantitatively the major reactions responsible for the chemical alteration of wellbore cement by CO_2 and H_2S and to predict the changes in porosity and permeability of wellbore cement under geologic sequestration conditions. The alterations in porosity and permeability of wellbore cement are important for assessing CO_2 and H_2S leakage risk along wellbores at a sequestration site. Compared with previous reactive transport modeling work,[22−24] the model presented in this paper is the first to simulate the interaction between pozzolan-amended wellbore cement and acid gas (CO_2 + H_2S). This model was calibrated against and used to help interpret experimental data obtained by scanning electron microscopy-backscattered electron (SEM-BSE) and scanning electron microscopy-energy dispersive spectroscopy (SEM-EDS) analyses for pozzolan-amended cement samples exposed to mixtures of CO_2 and H_2S under geologic sequestration conditions. The model allows consideration of effects of variation of pozzolan content in wellbore cement and variation of H_2S molar percentage in acid gas, which enables the simulation of a wide range of scenarios.

2. MODEL FORMULATION AND APPLICATION METHODS

2.1. Acid Gas Transport through Wellbore Cement under Geologic Sequestration Conditions. In geologic acid gas cosequestration conditions, wellbore cement is in contact with supercritical CO_2 and H_2S mixtures, brine saturated with CO_2 and H_2S, and caprock. Though caprock is not permeable to brine before injection of acid gas, the injection of acid gas can increase the pressure in the underlying reservoir, thus increasing the opportunity for brine in the reservoir to be pushed into the caprock and contact with wellbore annular cement (Figure 1).

This study investigated the potential for the transport of CO_2−H_2S saturated brine into the matrix of wellbore cement. If leakage occurs, flow of brine would be from the deep subsurface to the ground surface along or through a cemented wellbore, and the flow direction is in the upward direction (Figure 1).

There are two types of pathways considered for CO_2−H_2S saturated brine to transport in the cement.[24] If CO_2 and H_2S diffusion is from the bottom, the leaking flows will be in the same direction as the diffusion. In this case, the cement core consists of a series of zones with varying permeability values in the same direction as the flow. The fluid will need to flow through each zone. As a result, the effective permeability is typically controlled by the lowest permeability value in the domain. This effective permeability is referred to as "transverse permeability" (see Figure 1). If CO_2 and H_2S diffusion is from the side, the altered cement core consists of a series of zones with different permeability values in the direction vertical to the flow. In this case, the flow can preferentially flow through the local high permeability zones such as the degraded zone, and the flow will not go through zones with low permeability values such as those with calcite formation. As a result, the effective permeability is controlled by the largest permeability values in the domain. This effective permeability is referred to as "parallel permeability" (see Figure 1).

The effective permeability of wellbore cement can be calculated by dividing the cement into blocks, calculating local permeability of every block (as determined by porosity which changes with chemical reaction), and deriving effective permeability of the entire cement from local permeability values. In this work, the local permeability was calculated using a power law relating permeability to porosity:[24,25]

$$\frac{\mathrm{perm}_{i,t}}{\mathrm{perm}_{i,0}} = \left(\frac{\phi_{i,t}}{\phi_{i,0}}\right)^n \quad (1)$$

where $\mathrm{perm}_{i,t}$ is the local permeability value in the block i at time t; $\mathrm{perm}_{i,0}$ is the initial permeability; $\phi_{i,t}$ is the porosity value in the grid i at time t; $\phi_{i,0}$ is the initial porosity; and n is equal to 11. A n value of 11 is chosen according to previous modeling efforts by the authors,[24] and this value lies in the range of n values (3−75) reported in other articles.[26−30]

With local permeability values calculated from porosity values determined by physical-chemical modeling, the effective permeability of the entire cement can be calculated. The transverse effective permeability can be calculated using the classical formulation for flow resistance in series, and the parallel effective

dx.doi.org/10.1021/ef401749x | Energy Fuels 2013, 27, 6921−6937

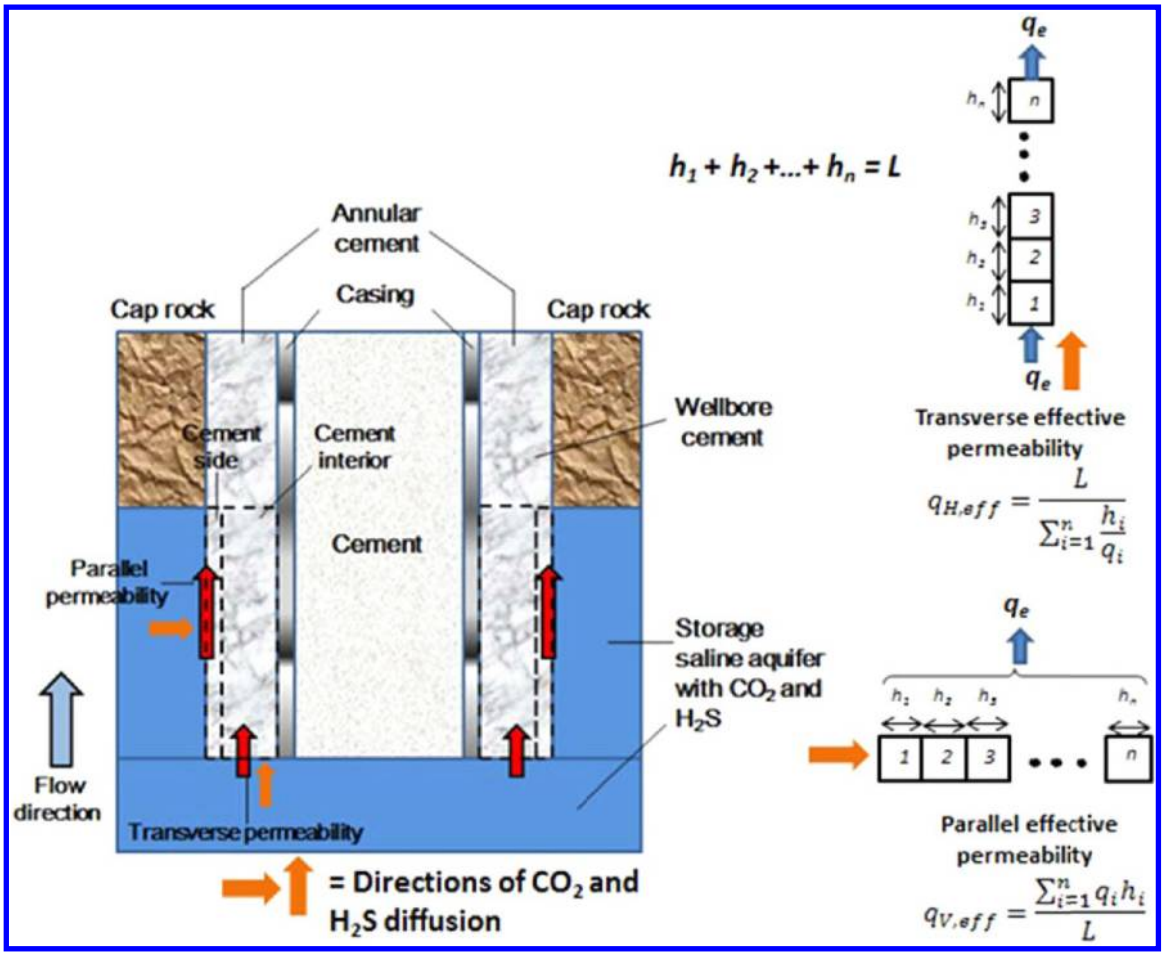

Figure 1. Schematic of transverse and parallel transport of brine saturated with CO_2 and H_2S through wellbore cement.

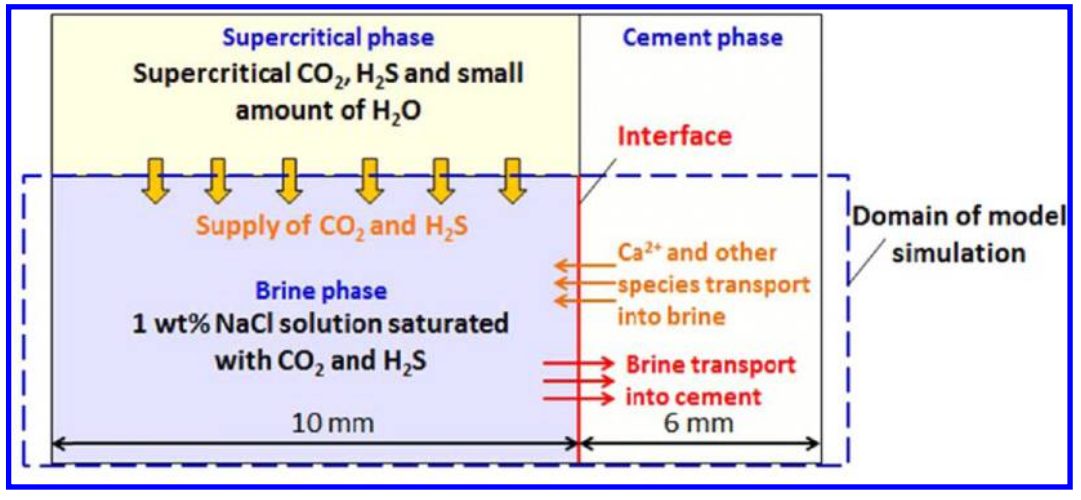

Figure 2. Schematic of the two-phase system at the cement−fluid interface modeled with CrunchFlow. Direct interaction of the supercritical phase with the cement was not incorporated into the reaction model.

permeability can be calculated using the classical formulation for flow resistance in parallel.[31]

Transverse effective permeability:

$$\text{perm}_{e,t} = \frac{L}{\sum_{i=1}^{n} \frac{h_i}{\text{perm}_{i,t}}} \quad (2)$$

where $\text{perm}_{e,t}$ is the transverse effective permeability at time t; L is the width of the model simulation domain for the cement (6 mm for the cement samples modeled here, see Figures 1 and 2); h_i is the length of the individual block (0.01 mm in the model); and $\text{perm}_{i,t}$ is the local permeability value in the block i at time t (see Figure 1).

dx.doi.org/10.1021/ef401749x | *Energy Fuels* 2013, 27, 6921−6937

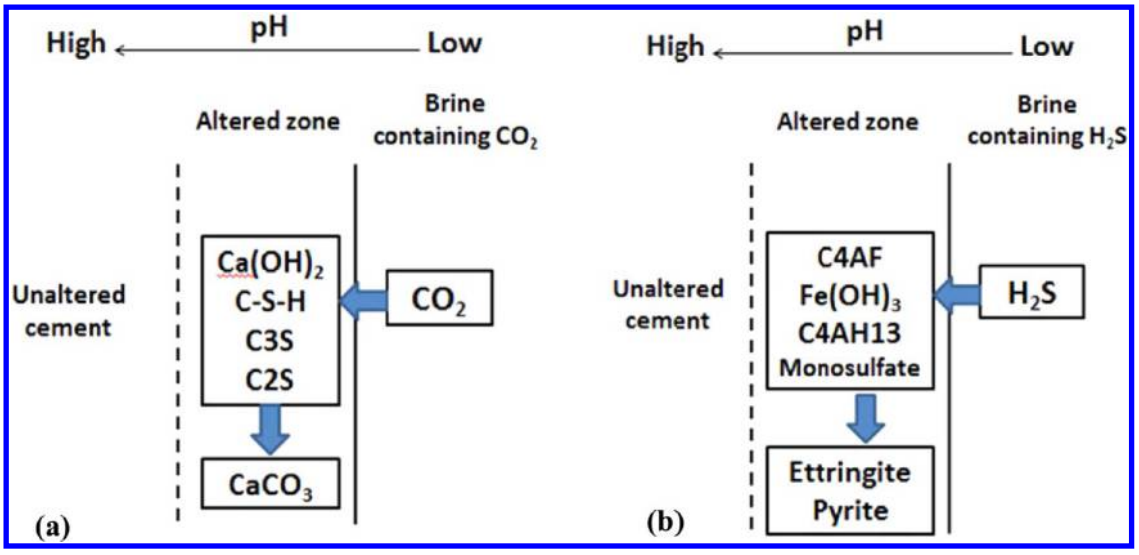

Figure 3. Schematic of (a) the interaction between CO_2 and pozzolan-amended cement, and (b) the interaction between H_2S and pozzolan-amended cement (b). Abbreviations of minerals: C3S = $3CaO{\cdot}SiO_2$, C2S = $2CaO{\cdot}SiO_2$, C4AF = $4CaO{\cdot}Al_2O_3{\cdot}Fe_2O_3$, and C4AH13 = $4CaO{\cdot}Al_2O_3{\cdot}13H_2O$.

Parallel effective permeability

$$\text{perm}_{e,t} = \frac{\sum_{i=1}^{n} \text{perm}_{i,t} h_i}{L} \quad (3)$$

where, $\text{perm}_{e,t}$ is the parallel effective permeability at time t; L is the width of the model simulation domain for the cement (6 mm for the cement samples modeled here, see Figures 1 and 2); h_i is the length of the individual block (0.01 mm in the model); and $\text{perm}_{i,t}$ is the local permeability value in the block i at time t (see Figure 1). Transverse effective permeability corresponds to flow through series (transverse) beds, and parallel effective permeability corresponds to flow through parallel beds.[31] The use of "transverse effective permeability" and "parallel effective permeability" is also consistent with the nomenclature used in previous work.[24]

The change in effective permeability compared with the original permeability (β) can be quantified by the following equation:

$$\beta_t = \frac{\text{perm}_{e,t}}{\text{perm}_{e,0}} \quad (4)$$

where $\text{perm}_{e,t}$ is the effective permeability at time t, and $\text{perm}_{e,0}$ is the effective permeability at time 0. It is important to note that $\text{perm}_{e,0} = \text{perm}_{i,0}$; i.e., the initial permeability is uniform throughout the sample.

In summary, both effective transverse and parallel permeability changes can be derived from porosity change, and porosity change is closely related to chemical reactions between wellbore cement and brine saturated with CO_2 and H_2S. To model these chemical reactions, a conceptual model and a reactive transport model based on the conceptual model were developed.

2.2. Conceptual Model To Describe Interactions between Pozzolan-Amended Cement and Acid Gas. The interaction between acid gas (CO_2 and H_2S) and pozzolan-amended wellbore cement in geologic carbon sequestration conditions is complex, involving many reactions, including the dissolution of Ca-bearing cement phases (portlandite, C−S−H, $3CaO{\cdot}SiO_2$, $2CaO{\cdot}SiO_2$, etc), precipitation and dissolution of carbonate minerals (calcite and aragonite), and formation of sulfur-bearing minerals (ettringite and pyrite). Figure 3 shows two simplified diagrams of the interactions between CO_2 and wellbore cement, and the interactions between H_2S and wellbore cement.

Table 1. Conditions Used for Experiments with Pozzolan-Amended Cement Samples Exposed to Acid Gas

parameter	value
temperature	50 °C
pressure	150 bar
CO_2 partial pressure	119 bar
$[CO_2]$ in brine	0.90 mol/L[a]
H_2S partial pressure	31 bar
$[H_2S]$ in brine	1.36 mol/L[b]
brine composition	1 wt % NaCl ($[NaCl] \approx 0.17$ mol/L)
initial pH (brine)	2.9[c]
initial pH (cement core)	8.0[d]
dimensions of cement samples	12 mm (diameter) × 60 mm (height)

[a]CO_2 concentration was obtained from ref 52 given the CO_2 partial pressure of 119 bar. [b]H_2S concentration was obtained from ref 53 given the H_2S partial pressure of 31 bar. [c]EERC was not able to get an in situ pH meter to measure the pH when the system was pressurized. Therefore, no experimental pH measurements were recorded. This value was obtained by calculation with the use of the Geochemist Workbench thermodynamic database.[7] [d]It is not possible to measure pH in cement core during the exposure experiment. A typical initial pH in cement core is 13.[54] However, the simulation crushed when this value was used. As a result, a lower initial pH (8.0) was assigned.

2.3. Development of a Reactive Transport Model Using CrunchFlow Based on the Conceptual Model. This section describes the development of a reactive transport model using the multicomponent reactive transport modeling software CrunchFlow[32] to model interactions of acid gas with pozzolan-amended cement. The model is developed based on the conceptual model represented in Figure 3, which describes how CO_2 and H_2S react with cement phases in pozzolan-amended wellbore cement. The developed reactive transport model allows the prediction of the temporal evolution of mineral volume percentage, porosity, and permeability of wellbore cement under geologic CO_2−H_2S cosequestration conditions.

2.3.1. Overview of Modeling Software CrunchFlow. The code for the multicomponent reactive transport model CrunchFlow

dx.doi.org/10.1021/ef401749x | Energy Fuels 2013, 27, 6921−6937

Table 2. Mineral Composition and Physical Properties of the 35:65 Pozolan-Amended Cement

mineral name	mineral formula	source	specific surface area (m^2/g)[h]	vol % (35:65 sample)
C3S	Ca_3SiO_5	unhydrated cement grain	0.5	3.7[a]
C2S	Ca_2SiO_4	unhydrated cement grain	0.5	1.1[a]
C4AF (Brownmill-erite)	$4(CaO)\cdot Al_2O_3\cdot Fe_2O_3$	unhydrated cement grain	10	0.9[a]
quartz	SiO_2	fly ash additive	0.1	3.6[a]
portlandite	$Ca(OH)_2$	hydration of cement	16.5	1.8[a]
ettringite	$Ca_6Al_2O_6(SO_4)_3\cdot 32H_2O$	hydration product of calcium sulfoaluminate in cement	9.8	1.0[a]
calcium silicate hydrate (am)	C−S−H (am)	hydration of C3S and C2S phases in cement	41.0	43.0[b]
silicon dioxide (am)	SiO_2 (am)	fly ash additive	0.1	10.3[c]
C4AH13 (am)	$(CaO)_4Al_2O_3\cdot 13H_2O$ (am)	hydration of C3A phase in cement	10	2.0[d]
monosulfate (am)	$(CaO)_3Al_2O_3(CaSO_4)\cdot 12H_2O$ (am)	hydration of monosulfoaluminate phases in cement	10	9.0[e]
amorphous iron hydroxide	$Fe(OH)_3$ (am)	hydration of C4AF in cement and Fe_2O_3 in fly ash additives	600	0.6[f]
		amorphous phase total		64.9
		crystalline phase total		12.1
		porosity		23.0[g]

[a]The weight percentages of all crystalline mineral phases were obtained by quantitative XRD analysis. The volume percentages of these crystalline minerals were calculated from the weight percentages, given molecular weights and molar volumes of these minerals. [b]The weight percentage of amorphous C−S−H was determined from total Ca wt % (SEM-EDS data) of the unexposed sample.

$$\text{wt \%(C - S - H)} = [\text{total Ca wt \%} - \sum \text{Ca wt \%}(i) \times \text{wt \%}(i)]/[\text{Ca wt \% (C - S - H)}]$$

where Ca wt %(i) is the Ca weight percentage in mineral i, i = C3S, C2S, C4AF, portlandite, ettringite, C4AH13 and monosulfate. wt %(i) is the weight percentage of mineral i in the sample. The volume percentage of C−S−H was calculated from the weight percentage of C−S−H, given molecular weight (196 g/mol[39]) and molar volume (84.7 cm^3/mol[39]) of C−S−H. [c]The volume percentage of SiO_2 (am) was determined after the volume percentages of all the other minerals were determined.

$$\text{vol \%}(SiO_2) = 1 - \sum \text{vol \%}(i) - \phi$$

where vol %(i) is the volume percentage of mineral i in the sample, and ϕ is porosity of the sample. [d]The weight percentage of C4AH13 was determined from total Al wt% (SEM-EDS data) of the unexposed sample.

$$\text{wt \%(C4AH13)} = [\text{total Al wt \%} - \sum \text{Al wt \%}(i) \times \text{wt \%}(i)]/[\text{Al wt\%(C4AH13)}]$$

where Al wt %(i) is the aluminum weight percentage in mineral i, i = C4AF, ettringite and monosulfate. wt %(i) is the weight percentage of mineral i in the sample. The volume percentage of C4AH13 was calculated from the weight percentage of C4AH13, given molecular weight (560 g/mol) and molar volume (274 cm^3/mol[55]) of C4AH13. [e]The weight percentage of monosulfate was determined from total S wt % (SEM-EDS data) of the unexposed sample.

$$\text{wt \%(monosulfate)} = [\text{total S wt \%} - \text{S wt \%(ettringite)} \times \text{wt \%(ettringite)}]/[\text{S wt \%(monosulfate)}]$$

where S wt %(ettringite) is the S weight percentage in ettringite, and wt%(ettringite) is the weight percentage of ettringite in the sample. The volume percentage of monosulfate was calculated from the weight percentage of monosulfate, given molecular weight (622 g/mol) and molar volume (309 cm^3/mol[55]) of monosulfate. [f]The weight percentage of $Fe(OH)_3$ (am) was determined from total Fe wt % (SEM-EDS data) of the unexposed sample.

$$\text{wt \%}(Fe(OH)_3,\ \text{am}) = [\text{total Fe wt \%} - \text{Fe wt \%(C4AF)} \times \text{wt \%(C4AF)}]/[\text{Fe wt \% }(Fe(OH)_3,\ \text{am})]$$

where Fe wt %(C4AF) is the Fe weight percentage in C4AF, and wt %(C4AF) is the weight percentage of C4AF in the sample. The volume percentage of $Fe(OH)_3$ (am) was calculated from the weight percentage of $Fe(OH)_3$ (am), given molecular weight (107 g/mol) and molar volume (34 cm^3/mol[55]) of $Fe(OH)_3$ (am). [g]The porosity of the unexposed 35:65 samples was obtained from BET analysis. Because of the size limitation of the test tube, samples were broken into chunks and were loaded into the tube for analysis. As BET analysis cannot measure the micropores, BET analysis might underestimate the total porosity of the unexposed sample, which can lead to an underestimate of permeability increase (an underestimate of porosity results in an underestimate of effective diffusion coefficient, and a subsequent underestimate of degradation rate).

dx.doi.org/10.1021/ef401749x | Energy Fuels 2013, 27, 6921−6937

Table 2. continued

[h]Literature reports in which the specific surface areas of minerals were obtained are as follows: (i) Specific surface area of $Ca(OH)_2$: 16.5 m^2/g;[39] (ii) specific surface area of $CaCO_3$: 1 m^2/g;[39] (iii) specific surface area of C−S−H (Ca:Si = 1.6): 41 m^2/g;[39] (iv) specific surface area of C3S: 0.5 m^2/g;[56] (v) specific surface area of C2S: 0.5 m^2/g (assumed to be the same as that of C3S); (vi) specific surface area of ettringite: 9.8 m^2/g;[39] (vii) specific surface area of C4AF: 10 m^2/g (default value for minerals with unknown specific surface areas in CrunchFlow); (viii) specific surface area of C4AH13: 10 m^2/g (default value for minerals with unknown specific surface areas in CrunchFlow); (ix) specific surface area of monosulfate: 10 m^2/g (default value for minerals with unknown specific surface areas in CrunchFlow); (x) specific surface area of FeS (am): 80 m^2/g;[57] (xi) specific surface area of gypsum: 10 m^2/g (default value for minerals with unknown specific surface areas in CrunchFlow); (xii) specific surface area of $Fe(OH)_3$ (am): 600 m^2/g;[58] (xiii) specific surface area of quartz: 0.1 m^2/g;[39] (xiv) specific surface area of SiO_2 (am): 0.1 m^2/g (assumed to be the same as that of quartz).

Table 3. Pure-Water Diffusion Coefficients of Aqueous Species in the Cement−Brine System

species	D_0 (10^{-5} cm^2/s, T = 298 K)	D_0 (10^{-5} cm^2/s, T = 323 K)[f]
H^+	9.31[a]	16.79
Ca^{2+}	0.79[a]	1.42
OH^-	5.28[a]	9.52
SO_4^{2-}	1.06[a]	1.91
Fe^{2+}	0.67[b]	1.21
Fe^{3+}	0.7[c]	1.23
Na^+	1.33[a]	2.34
Cl^-	2.03[a]	3.57
HS^-	1.73[a]	3.08
S^{2-}	1.38[e]	2.41
HCO_3^-	1.185[d]	2.11
CO_3^{2-}	0.923[d]	1.65
Al^{3+}	0.541[d]	0.965
CO_2		3.77[g]
H_2S		3.84[g]

[a]Values are from ref 59. [b]The value is the average of two experimental measurements generated by refs 60 and 61. [c]The value is from ref 62. [d]Values are from ref 63. [e]Assumed to be 80% of the diffusivity of HS^-. [f]Except for CO_2 and H_2S, values at T = 323 K were obtained from an approximate correlation between diffusivity and temperature: $(D_i(T_1))/(D_i(T_2)) = (T_1\mu(T_2))/(T_2\mu(T_1))$. This relationship is derived from Einstein and Stokes equation: $D_i(T) = (kT)/(6\pi\mu(T)r_i)$. [g]Values were directly calculated from Wilke and Chang's equation.[40]

was developed at Lawrence Berkeley National Laboratory.[32,33] CrunchFlow is used to simulate reactive transport through porous media. It has been applied to complex multiphase systems.[34,35] The model is suitable to simulate interaction between pozzolan-amended wellbore cement and acid gas (CO_2 + H_2S), as it is able to simulate temporal evolution of aqueous species and solid minerals resulting from chemical reactions between wellbore cement and acid gas, and correlate the evolution with porosity and permeability changes of cement. A limitation of CrunchFlow is that it can only model single phase flow, which means the code cannot model supercritical CO_2−water two-phase flow systems. In addition, as only the water phase is considered, the model cannot simulate direct interactions between supercritical CO_2 and mineral phases. As a result, only the interaction between pozzolan-amended wellbore cement and acid gas dissolved in brine was simulated in this study.

2.3.2. Simulation Domain and Conditions. In geologic acid gas cosequestration conditions, wellbore cement is exposed to two different environments: supercritical CO_2 and H_2S liquid, and brine saturated with CO_2 and H_2S (Figure 2). In this work, only the interaction between wellbore cement and brine saturated with CO_2 and H_2S was modeled. An important assumption of the modeling work was that the rate of CO_2 and H_2S consumption caused by interaction between CO_2/H_2S and cement was less than the rate of CO_2 and H_2S supply from supercritical liquid. Thus, the CO_2 and H_2S concentrations in the bulk brine were considered constant and always the same as the initial CO_2 and H_2S concentrations (see Figure 2).

The model was applied to describe experimental results obtained from exposure of cylindrical pozzolan-amended cement samples exposed to CO_2−H_2S mixtures under geologic sequestration conditions.[18] The cement used in the experiments was 35 vol % pozzolan + 65 vol % Class H Portland cement (hereafter referred to as 35:65 sample). To prepare pozzolan-amended cement samples, Class H Portland cement was mixed with pozzolan (Class F fly ash, with ∼70 wt % silica, alumina and Fe_2O_3, ∼5 wt % sulfate, and less than 20 wt % CaO) according to American Petroleum Institute (API) Recommended Practice (RP) 10B 201 (section 17.4).[36] The slurry density for the 35:65 samples prepared was 1.74 g/cm^3. After 28 days of curing, samples were placed in glass vials filled with 1 wt % NaCl solution, and the glass vials were placed in a high-pressure stainless steel vessel. During the exposure experiments, the vessel was filled with supercritical CO_2 and H_2S, and the solution in glass vials was saturated with CO_2 and H_2S. Details of sample preparation and exposure experiments can be found in other reports.[6,18] A summary of the experimental conditions is provided in Table 1, and the mineral composition of the 35:65 sample is provided in Table 2.

2.3.3. Important Equations and Parameters Used in Model Simulation. The mass conservation equations for chemical species undergoing transport are the fundamental equations upon which CrunchFlow is based. The expression of mass conservation equation for species i is given by (revised from Steefel and Lasaga[37]):

$$\frac{\mathrm{d}(\phi C_i)}{\mathrm{d}t} = \underbrace{\frac{\mathrm{d}}{\mathrm{d}x}\left(\phi D_{ie}\frac{\mathrm{d}C_i}{\mathrm{d}x}\right)}_{\text{diffusion term}} - \underbrace{\frac{\mathrm{d}}{\mathrm{d}x}(\phi u C_i)}_{\text{advection term}} \pm \underbrace{\sum_{i=1}^{N} v_{ir}R_{ir}}_{\text{reaction term}} \quad (5)$$

where ϕ is the porosity of the system (unitless), C_i is the concentration of species i (mol/m^3), D_{ei} is the effective diffusion coefficient of species i (m^2/s), u is flow velocity (m/s), R_{ir} is the rth reaction rate that can produce or consume species i ($mol/m^3 s$) and v_{ir} is stoichiometric number of species i in the rth reaction (unitless). It is important to note that for the cement system a static, no-flow condition was assumed, and therefore the advection term was set equal to 0 (u = 0).

Given the values of the three parameters (ϕ, D_e, and R) in eq 5, Crunchflow can solve the mass conservation equation and generate concentration profiles of all species i as a function of time and space. The details for calculation of these parameters are described below.

ϕ-Porosity of Cement. The porosity of the cement matrix can be expressed as a function of the volume fractions of all mineral phases:[38]

$$\phi(t) = 1 - \sum_{i=1}^{m} \mathrm{fr}_i(t) - \mathrm{fr}_n \quad (6)$$

dx.doi.org/10.1021/ef401749x | Energy Fuels 2013, 27, 6921−6937

Table 4. All Reactions Considered for CO_2−Cement Interaction[a]

Reaction #	Reaction formula	K_{eq} (50°C)	$\sum_{l=1}^{M} k_l(\prod_{i=1}^{N} a_i^{Pi})$ mol/(m²s) (50 °C)
(1)	$Ca(OH)_2(s) + 2H^+ \leftrightarrow Ca^{2+} + 2H_2O$ Portlandite dissolution	$10^{21.05}$	$10^{-7.2}[H^+]^{0.5}$
(2)	$CaCO_3(s) + H^+ \leftrightarrow Ca^{2+} + HCO_3^-$ Calcite precipitation and dissolution	$10^{1.31}$	$10^{-3}[H^+]$ (dissolution) $10^{-8.3}[Ca^{2+}][HCO_3^-]$ (precipitation)
(3)	$C-S-H(Ca:Si=1.6)(s) + 3.2H^+ \leftrightarrow 1.6Ca^{2+} + 4.18H_2O + SiO_2(s,am)$ C-S-H dissolution	$10^{26.19}$	$10^{-11.56} + 10^{-4}[H^+]$
(4)	$Ca_3SiO_5(s) + 6H^+ \leftrightarrow 3Ca^{2+} + SiO_2(s,am) + 3H_2O$ Dissolution of unhydrated C3S phase	$10^{70.29}$	$10^{-7} \times [H^+]^{0.465} \times [CaOH^+]^{-0.33}$
(5)	$Ca_2SiO_4(s) + 4H^+ \leftrightarrow 2Ca^{2+} + SiO_2(s,am) + 2H_2O$ Dissolution of unhydrated C2S phase	$10^{39.46}$	10^{-12}
(6)	$CO_2(aq) + H_2O \leftrightarrow H^+ + HCO_3^-$ CO_2 (aq)—HCO_3^- conversion reaction	$10^{-6.23}$	Fast reaction
(7)	$HCO_3^- \leftrightarrow H^+ + CO_3^{2-}$ $HCO_3^- - CO_3^{2-}$ conversion reaction	$10^{-10.13}$	Fast reaction

[a]Note: Please refer to Supporting Information to see the details of K_{eq} and reaction rate calculations for all reactions listed in Table 4.

where $\phi(t)$ is the porosity of cement at time t, $fr_i(t)$ is the volume fraction of reactive mineral phase i at time t and fr_n is the volume fraction of all inert mineral phases in cement. CrunchFlow calculates the volume fractions of all reactive mineral phases, based on the dissolution/precipitation reactions occurring for the reactive mineral phases.

D_{ei} – Effective Diffusion Coefficient of Species i. Calculation of effective diffusion coefficients requires aqueous diffusion coefficients in aqueous species, tortuosity, and porosity. The equation used to calculate the effective diffusion coefficient of species i is given by[39]

$$D_{ei} = D_{0i} T \phi \tag{7}$$

where, D_{0i} is the diffusion coefficient of species i in pure water. Pure-water diffusion coefficients of charge-neutral species (e.g., CO_2 and H_2S) can be evaluated by the Wilke—Chang equation,[40] and pure-water diffusion coefficients of charged species can be obtained from the literature. Table 3 summarizes the pure-water molecular diffusion coefficients of all aqueous species considered in the modeling. T is the reciprocal of tortuosity. In this work, tortuosity was defined as the length of the pathway divided by the shortest distance between the termini of the pathway. This is the most common way to define tortuosity, though some investigators have defined tortuosity as the shortest distance between the ends of the pathway divided by the length of the pathway. In this work, T was set equal to 0.004, which is within the range of reported values for cement.[41,42] It is important to note that the T value of 0.004 is for unreacted cement, and the model is not able to automatically update the T value as a function of exposure time. The inability of the model to produce time-dependent T value is a limitation for the model, given the inward precipitation/dissolution of the calcium carbonate layer through the reaction zone as the reaction front ingresses into the cement, which might change the value of T.

R_{ir}-Reaction Rate of Species i in rth Reaction. R_{ir} is the overall reaction rate of reaction r that can produce or consume species i. CrunchFlow assumes that mineral dissolution and precipitation reactions are the rate-limiting reactions, while reactions involving aqueous species only (except for oxidation—reduction reactions) are fast reactions. The mineral dissolution/precipitation rate law is given by Steefel:[32]

$$R_{ir} = A\left(\sum_{l=1}^{M} k_l\left(\prod_{i=1}^{N} a_i^{p_i}\right)\right)\left(1 - \frac{Q}{K_{eq}}\right) \tag{8}$$

where A is the surface area (m^2/m^3 porous media) of the mineral involved in the reaction, k_l is the lth parallel reaction rate ($mol/m^2 \cdot s$) that contributes to the dissolution/precipitation of the mineral, $\Pi_{i=1}^{N} a_i^{p_i}$ describes the effects of various ions in solution on the dissolution/precipitation rate of parallel reaction l (k_l), Q is the reaction quotient, and K_{eq} is the reaction equilibrium constant. The reaction quotient (Q) is equal to the product of concentrations of aqueous species in the product side of the reaction divided by the product of concentrations of aqueous species in the reactant side of the reaction. For example, given the calcite dissolution reaction,

$$CaCO_3(s) + H^+ = = Ca^{2+} + HCO_3^- \tag{9}$$

Q is equal to $([Ca^{2+}]\,[HCO_3^-])/([H^+])$, and the concentrations of all aqueous species are calculated by CrunchFlow.

The ratio of Q to K_{eq} determines the direction of the reaction. Taking eq 9 as an example, If Q is higher than K_{eq}, then the system is supersaturated with Ca^{2+} and HCO_3^-, and the reaction will become calcite precipitation reaction.

It is important to note that there are uncertainties associated with eq 8, and the uncertainties mainly stem from the lack of reliable information on the values of initial mineral reactive surface areas (mineral surface areas are updated in CrunchFlow

dx.doi.org/10.1021/ef401749x | Energy Fuels 2013, 27, 6921−6937

Table 5. All Reactions Considered for H_2S–Cement Interaction[a]

Reaction #	Reaction formula	K_{eq} (50 °C)	$\sum_{l=1}^{M} k_l(\prod_{i=1}^{N} a_i^{pi})$ mol/(m²s) (50 °C)
(8)	$Ca_6Al_2O_6(SO_4)_3 \cdot 32H_2O(s) + 12H^+ \leftrightarrow 6Ca^{2+} + 2Al^{3+} + 3SO_4^{2-} + 38H_2O$ Dissolution and precipitation of ettringite	$10^{57.67}$	7.952×10^{-12}
(9)	$4CaO \cdot Al_2O_3 \cdot Fe_2O_3(s) + 20H^+ \leftrightarrow 4Ca^{2+} + 2Al^{3+} + 2Fe^{3+} + 10H_2O$ Dissolution and precipitation of C4AF (Brownmillerite)	10^{121}	10^{-12}
(10)	$(CaO)_4 Al_2O_3 13H_2O(s) + 14H^+ \leftrightarrow 4Ca^{2+} + 2Al^{3+} + 20H_2O$ Dissolution of C4AH13 phase	$10^{94.89}$	10^{-12}
(11)	$(CaO)_3 Al_2O_3 (CaSO_4) \cdot 12H_2O(s) + 12H^+ \leftrightarrow 4Ca^{2+} + 2Al^{3+} + SO_4^{2-} + 18H_2O$ Dissolution and precipitation of monosulfate	$10^{66.02}$	10^{-12}
(12)	$Fe^{2+} + HS^- \leftrightarrow FeS(s,am) + H^+$ Amorphous FeS formation	$10^{4.74}$	$10^{-8.9}$
(13)	$FeS(s,am) + H_2S \leftrightarrow FeS_2(s) + H_2$ Pyrite formation	$10^{5.02}$	$4.08 \times 10^{-8} \times [H_2S]$
(14)	$SO_4^{2-} + Ca^{2+} + 2H_2O \leftrightarrow CaSO_4 \cdot 2H_2O(s)$ Gypsum formation	$10^{4.61}$	10^{-6}
(15)	$8Fe(OH)_3(s) + HS^- = 8Fe^{2+} + SO_4^{2-} + 5H_2O + 15OH^-$ Dissolution of $Fe(OH)_3$ phase: sulfate formation	$10^{109.7}$	$10^{-10}[HS^-]$
(16)	$2Fe(OH)_3(s) + 3H_2S = S^0(s) + FeS(s) + 6H_2O$ Dissolution of $Fe(OH)_3$ phase: Elemental sulfur formation	$10^{2.26}$	$10^{-8} \times [H_2S]$
(17)	$H_2S \leftrightarrow H^+ + HS^-$ Dissociation of H_2S	$10^{-6.69}$	Fast reaction
(18)	$HS^- \leftrightarrow H^+ + S^{2-}$ Dissociation of HS^-	$10^{-12.23}$	Fast reaction

[a]Note: Please refer to Supporting Information to see the details of K_{eq} and reaction rate calculations for all reactions listed in Table 5.

as a function of time using a simple equation (eq 10)[32]), and the variation of reaction rate constants over large span of Gibbs free energy of reaction.[23] As a result, values of A and k_l's in eq 8 obtained from literature may not fit a particular system of interest. In this work, a data fitting process was conducted to obtain appropriate k_l values, and some k_l values were adjusted from initial values found in the literature. Final k_l values can be found in Tables 4 and 5, and the processes to obtain final k_l values can be found in Supporting Information (Section S-3).

$$A_s(t) = A_s(0)\left(\frac{\phi_t}{\phi_0}\right) \tag{10}$$

where $A_s(t)$ is the surface area at time t, $A_s(0)$ is the initial surface area, ϕ_t is the porosity at time t, and ϕ_0 is the initial porosity.

2.3.4. List of Reactions in the Model and Values of Reaction Parameters. Tables 4 and 5 show complete lists of reactions involved in CO_2—pozzolan-amended cement interaction and H_2S—pozzolan-amended cement interaction.

2.3.5. Model Outputs and Validation of Model Outputs. The simulation was conducted with 1-D transport for a domain with an overall length of 16 mm. The domain comprised 1600 grid blocks with a resolution of 0.01 mm. The domain included 6 mm of cement, consistent with the radius of the experimental cement cylinder, and the remaining 10 mm was specified as the CO_2 and H_2S saturated brine (see Figure 2). The 1-D model can produce calcite volume percentage, total Ca and S weight percentages in the solid phase, porosity and permeability at every block. With a block size of 0.01 mm, there were 600 blocks in the entire cement sample modeling domain from the surface to the interior of pozzolan-amended cement sample.

The outputs of the model were validated by data from acid gas exposure experiments conducted by Energy & Environmental Research Center (EERC), University of North Dakota. Experimental details can be found in Hawthorne et al.[6] and Zhang et al.[18] To enable comparison with data from the exposure experiments (samples were exposed for 2.5, 28, and 90 days in these experiments), model simulation results for 2.5, 28, and 90 days of exposure were obtained. Porosity and effective permeability simulation results of samples after 1 year and 30 years were also calculated, so as to evaluate the potential for acid gas leakage after longer times of exposure.

dx.doi.org/10.1021/ef401749x | Energy Fuels 2013, 27, 6921–6937

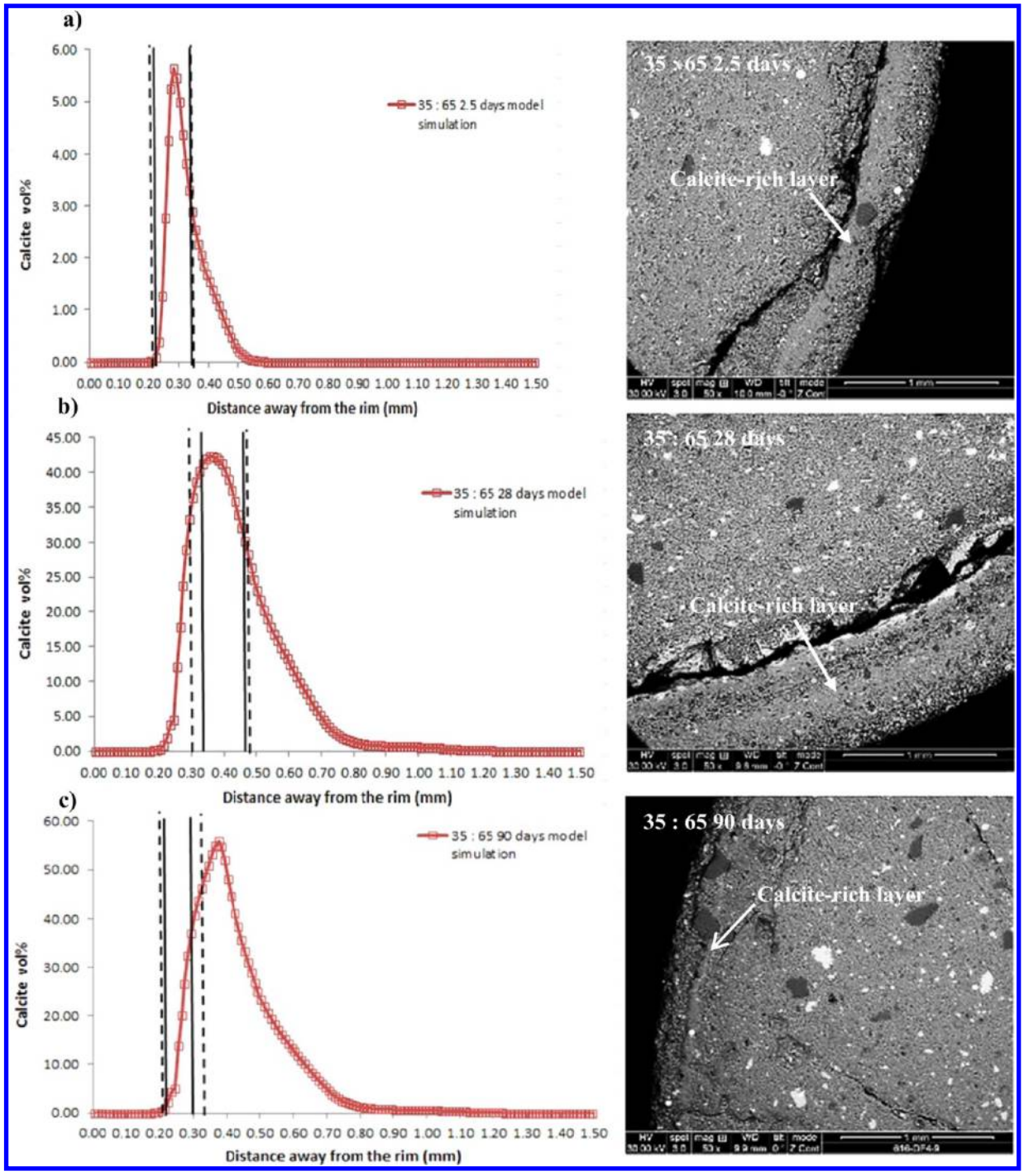

Figure 4. Comparison between calcite volume % model simulation results and calcite-rich layer location data obtained from SEM-BSE images. (a) 2.5 days of exposure; (b) 28 days of exposure; (c) 90 days of exposure. Black solid lines represent boundaries of the calcite-rich layer in SEM-BSE images, and black dashed lines represent the uncertainties of location measurement of the calcite-rich layer. Sample: 35:65 sample exposed to 1 wt % NaCl solution saturated with 79 mol % CO_2 and 21 mol % H_2S. The calcite-rich layer in the 90-day sample was thinner than that in 2.5-day and 28-day samples, which might be attributed to the compression of the calcite layer due to the discrepancy between the Young's moduli for the calcite layer and the Young's moduli for the unaltered cement.

The model was calibrated by matching the modeling output to the experimental observations of the solid phases and mineral composition after the cement samples were exposed to CO_2 and H_2S for different times.[18] The SEM-BSE images gave the location of calcite-rich layer, which was used to compare with the modeling output of the calcite volume percentage. The SEM-EDS analyses gave data for spatial distribution of total Ca wt % and total S wt % in the solid phase from the brine−cement interface to the interior of the sample, which were used to compare with model simulation output. Several key parameters, including the kinetic rate constants k for calcite precipitation, C−S−H dissolution, C3S dissolution, and $Fe(OH)_3$ dissolution, were adjusted to match the SEM-BSE and SEM-EDS data. Results from some key adjustment processes are provided in Figures S-1 to S-4 in Supporting Information.

dx.doi.org/10.1021/ef401749x | *Energy Fuels* 2013, 27, 6921−6937

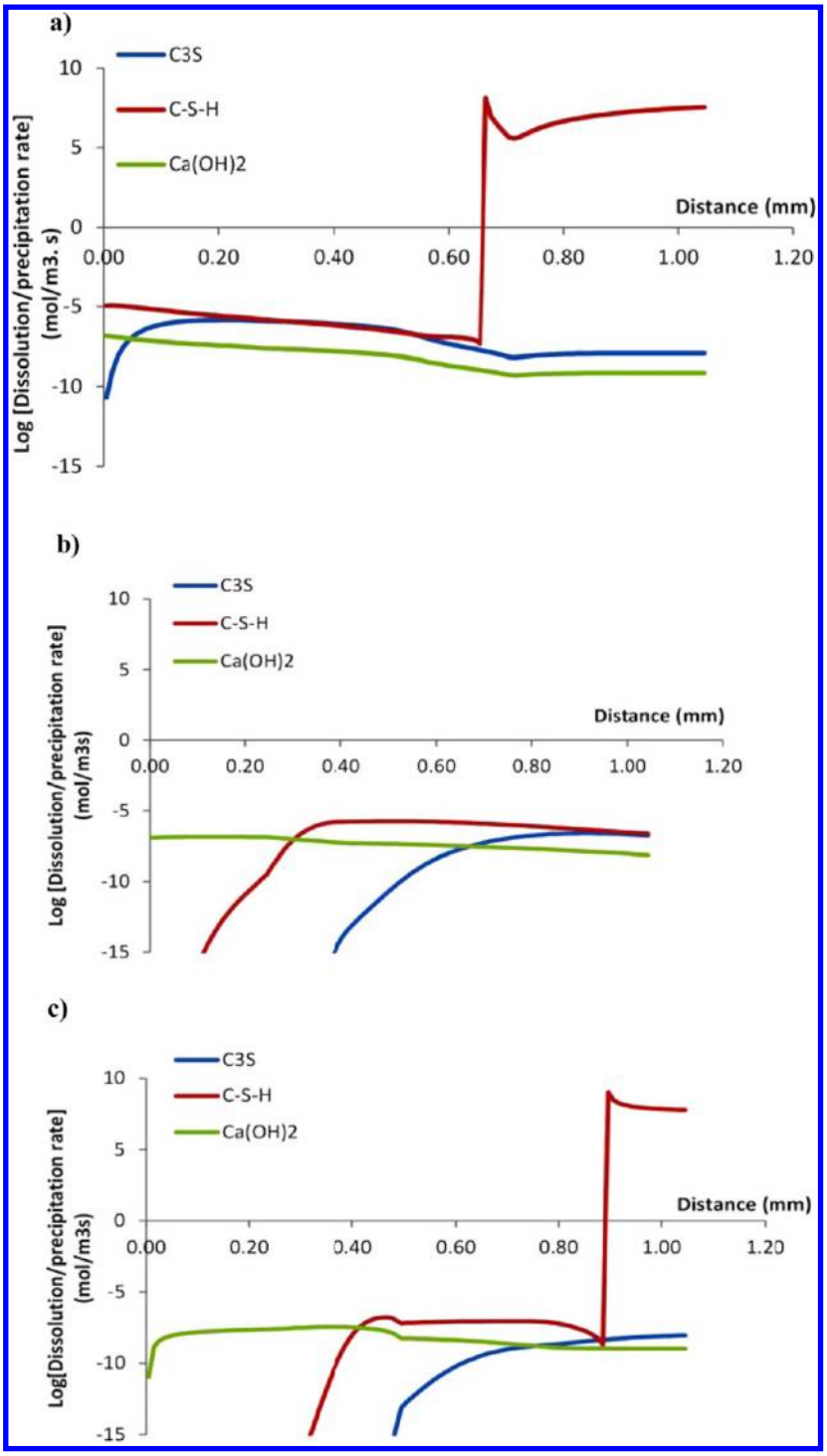

Figure 5. Simulated dissolution and precipitation rates (in log scale) of three minerals (C3S, C−S−H, and $Ca(OH)_2$) as a function of the distance away from the surface of the sample. (a) 35:65 sample exposed for 2.5 days; (b) 35:65 sample exposed for 28 days; (c) 35:65 sample exposed for 90 days. Negative values correspond to dissolution rate values ($\log(k_{dis})$, the higher the dissolution rate, the closer the value to 0), and positive values correspond to precipitation rate values ($-\log(k_{pre})$, the higher the precipitation rate, the closer the value to 0).

3. RESULTS AND DISCUSSION

3.1. Calcite vol % Results. Figure 4 shows the calcite vol % results for the 35:65 sample obtained from model simulation. The calcite vol % results were validated by comparison with the observed location of the calcite-rich layer obtained from SEM-BSE imaging. Locations of the calcite-rich layer were obtained by measuring the distances between the interface and the boundaries of the calcite-rich layer in SEM-BSE images. To ensure the accuracy of the measurements, four measurements of the location of the calcite-rich layer were made for every sample (e.g., four SEM-BSE images for each sample), and the average value of the four measurements was used as the final location value. It is important to note that in the case of 90 days (Figure 4c), the T value in eq 7 in the simulation domain of 0 mm to 0.5 mm was reduced from 0.004 to 0.0001 after 28 days of exposure. A T value of 0.0001 was chosen, because the simulation

dx.doi.org/10.1021/ef401749x | *Energy Fuels* 2013, 27, 6921−6937

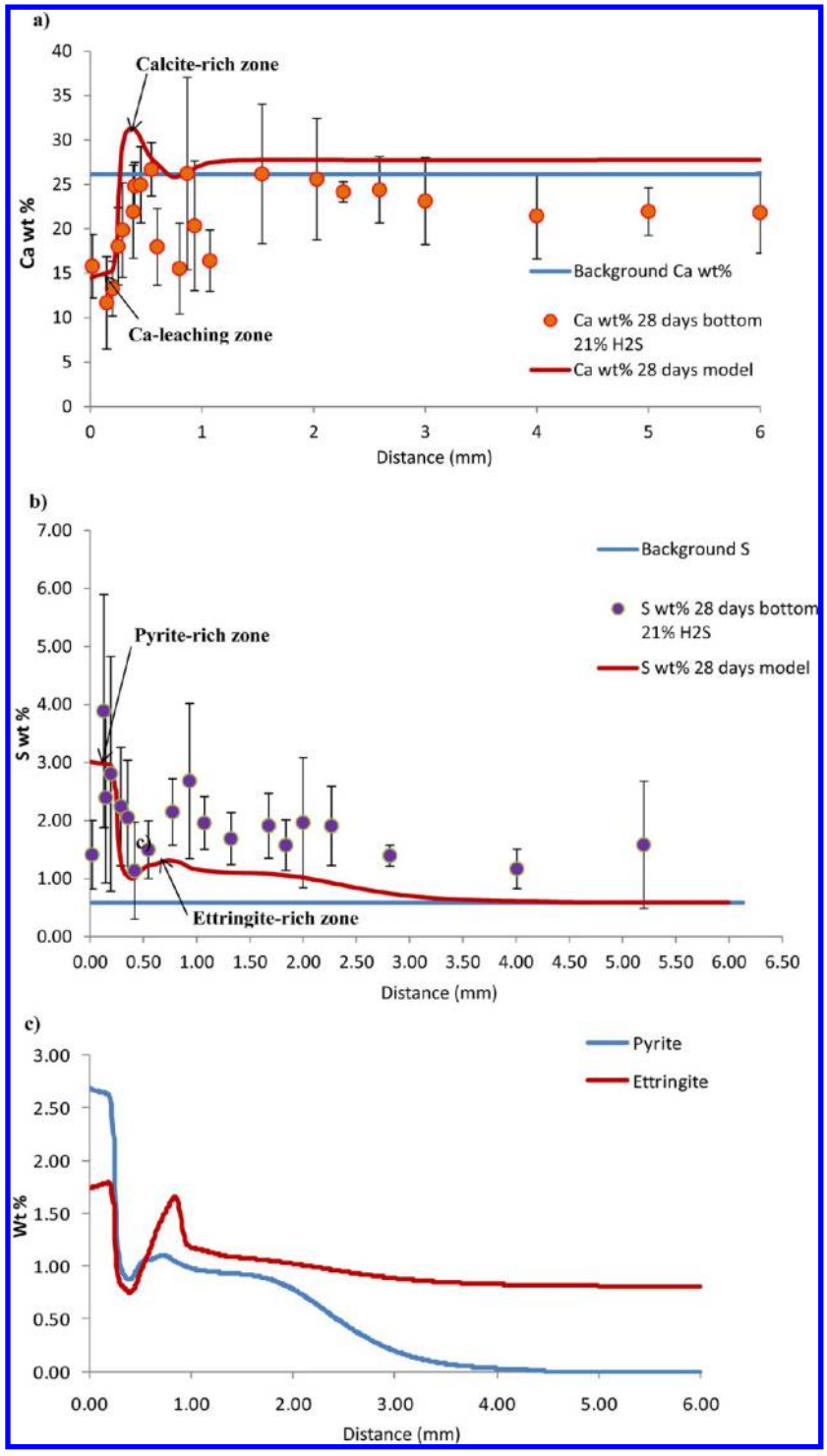

Figure 6. Comparison between model simulation and SEM-EDS analysis for total Ca and S wt %. (a) Ca wt % of the 35:65 sample exposed for 28 days; (b) S wt % of the 35:65 sample exposed for 28 days; (c) simulated pyrite and ettringite formation of the 35:65 sample exposed for 28 days. The results of samples exposed for 2.5 days and 90 days are provided in Supporting Information.

with a T value of 0.0001 produced a calcite-rich layer that is closest to the location of the calcite-rich layer from SEM-BSE observation among all T values tested (0.004, 0.001, 0.0001, and 0.00001). The reduction of T value (corresponding to an increase in tortuosity) is consistent with experimental observation from other studies,[42] which showed that the formation of calcite increased tortuosity of the calcite-rich zone in the cement mortar.

The predicted calcite vol % on day 2.5 and day 28 (Figure 4a,b) were consistent with SEM-BSE imaging data. As to the calcite vol % result of the 90-day sample (Figure 4c), the calcite peak predicted by the model was at 0.4 mm, while the calcite-rich zone obtained from SEM-BSE imaging was between 0.2 mm and 0.3 mm. Simulation results show that the calcite-rich layer built up rapidly after a relatively short time of exposure (the peak calcite vol% increased from 5.5% after 2.5 days of exposure to

dx.doi.org/10.1021/ef401749x | *Energy Fuels* 2013, 27, 6921−6937

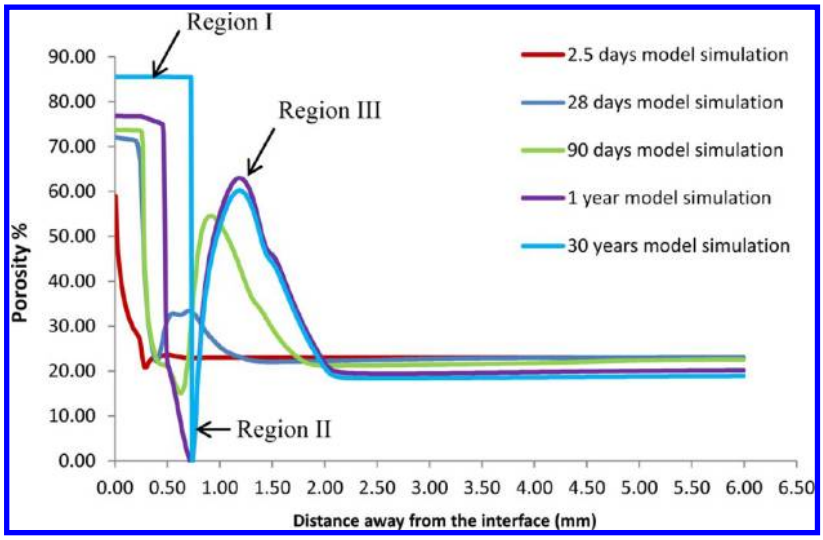

Figure 7. Porosity changes from the interface region to the interior of the 35:65 sample after 2.5 days, 28 days, 90 days, 1 year, and 30 years of exposure.

42% after 28 days of exposure). Further movement of calcite-rich layer to the interior from 28 days of exposure to 90 days of exposure was suppressed. Two factors result in a slower movement of the calcite-rich layer to the interior of the samples after 28 days of exposure. The first factor is that the cement comes close to equilibrium with the fluid with the increase of exposure time in a batch system, thus the calcite precipitation reaction becomes slow. Different from batch system, experiments conducted in a flow-through system show deeper reaction fronts into the interior of samples,[43−45] as the fluid is continually replaced in a flow-through system, and equilibrium may not be fully reached. Therefore, if the experiments in this work presented here had been conducted in a flow-through system, the calcite peak might have moved further into the sample (deeper than 0.4 mm) after 90 days of exposure. The second contributor is the clogging of pore spaces by calcite and subsequent blockage of CO_2 penetration to the interior.

The formation of a calcite-rich layer is typically cited as a means to reduce the porosity of cement and contribute to the "self-sealing" of cement.[46,47] However, Barlet-Gouédard et al.,[48] Fabbri et al.,[49] and Gherardi et al.[23] reported that formation of cracks and significant strength loss were usually recognized in association with extensive carbonation processes. In the modeling performed here, the extensive carbonation at the surface of the pozzolan-amended cement was predicted to occur rapidly (after 28 days of exposure), which may lead to crack formation and strength loss of the pozzolan-amended cement. To be specific, the Young's moduli for the calcite layer was reported to be lower than that of the unreacted cement.[44,45] After 7 days of exposure to CO_2, the average Young's moduli decreased from 28 ± 7 GPa in the unaltered cement to 18 ± 3 GPa in the carbonate layer.[45] The discrepancy between the Young's moduli for the calcite layer and the Young's moduli for the unaltered cement may result in compression of the calcite layer,[44] which can be observed in the SEM-BSE image of the 90-day sample (Figure 4).

The dissolution of Ca-bearing cement materials is the main source of Ca^{2+} to form calcite. For pozzolan-amended cement, the modeling indicated that C−S−H, C3S, and $Ca(OH)_2$ were the three minerals that provided most of dissolved Ca^{2+} to form calcite. Figure 5 shows that the spatial distribution of the simulated dissolution rates of C−S−H, C3S, and $Ca(OH)_2$ in the 35:65 sample at different exposure times. It can be seen that C−S−H was the most important Ca^{2+} source from 2.5 days to 90 days of exposure. C3S was also an important Ca^{2+} source in the early times (2.5 days), while not at later times because all the C3S in the sample was dissolved and did not contribute to the production of Ca^{2+}. The dissolution rate of $Ca(OH)_2$ was relatively stable from 2.5 days to 90 days of exposure. As the $Ca(OH)_2$ dissolution rate was not high, the dissolution of $Ca(OH)_2$ could last for a long time. After 90 days of exposure, $Ca(OH)_2$ was still dissolving in the region very close to the interface (0 to 0.3 mm), while C3S and C−S−H had completely dissolved.

3.2. Total Ca wt % (Solid Phase). Figure 6a compares total Ca wt % (solid phase) from the model output and the sample analysis results obtained from SEM-EDS analysis after 28 days of exposure to acid gas. SEM-EDS analysis results of Ca wt % were recorded as a function of the distance away from the interface, and at each distance, 20 measurements were made at 20 spots of the sample (all 20 spots had the same distance to the interface), and the total Ca wt% was the average of the 20 measurements. In the model simulation, total Ca wt% was calculated by

$$\text{total Ca wt\%} = \sum_{i=1}^{n} \text{Ca}(i) \times \text{wt\%}(i) \tag{11}$$

where $\text{Ca}(i)$ is the calcium wt % in mineral i (mass fraction), and wt %(i) is the wt % of mineral i in the sample.

Although the model slightly overpredicted the absolute values, the model simulation results were consistent with the trend indicated by the SEM-EDS data as evident in Figure 6a. Simulation results show a Ca-leaching zone right at the brine-cement interface, a calcite-rich zone at about 0.3 mm, which is consistent with the observed Ca peak. Over time (2.5-day and 90-day results can be found in Figure S-5 in Supporting Information), the Ca-leaching zone in the interface region expanded and the calcite-rich zone moved toward the interior. The moving of the calcite-rich zone from the exterior to the interior is consistent with observation of the calcite-rich zone from other studies of CO_2-cement interactions.[23,24] For example, calcite precipitation was observed in the region 0.2 m away from cement interface after about 50 years of exposure,[23] and the location of the calcite-rich region moved from 0.23 mm away from interface after 23 days of

dx.doi.org/10.1021/ef401749x | Energy Fuels 2013, 27, 6921−6937

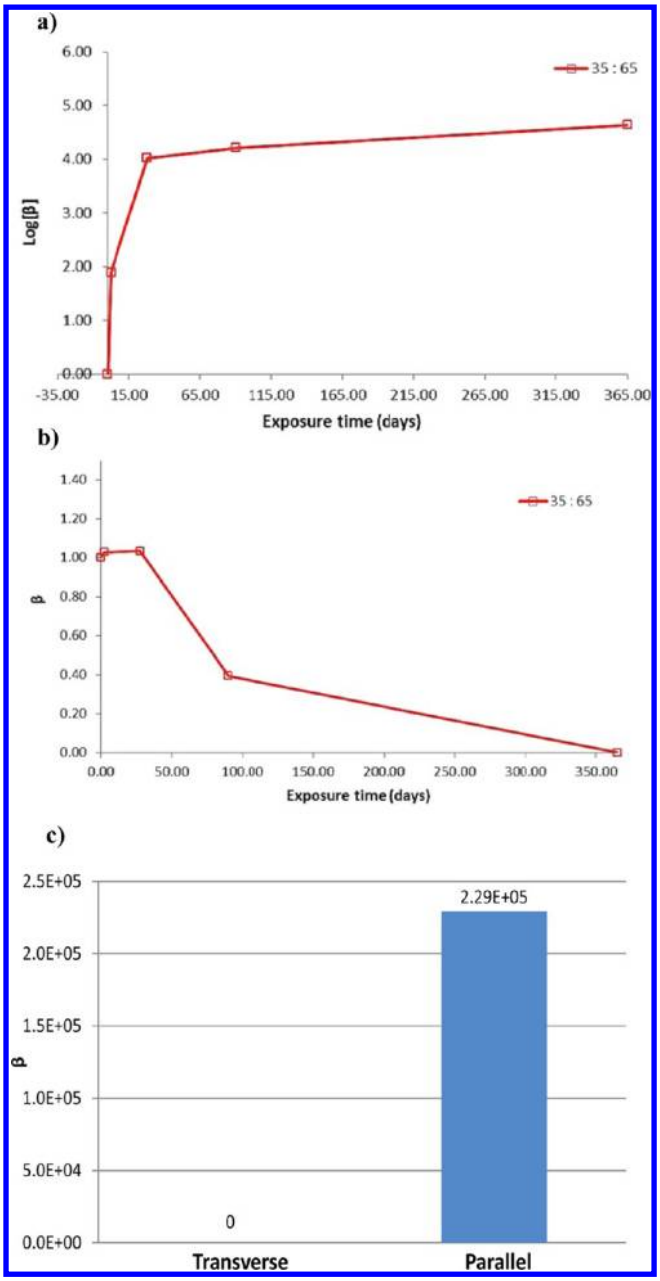

Figure 8. (a) Change in effective parallel permeability of the 35:65 sample from 0 to 365 days of exposure; (b) change in effective transverse permeability of the 35:65 sample from 0 to 365 days of exposure; (c) change in effective transverse and parallel permeabilities of the 35:65 sample after 30 years of exposure. $\beta_t = \text{perm}_{e,t}/\text{perm}_{e,0}$.

exposure to 0.42 mm away from interface after 90 days of exposure.[24]

3.3. Total S wt %. Figure 6b shows total S wt % (solid phase) model simulation results and data obtained from SEM-EDS analysis for 28 days.

In model simulation, total S wt% was calculated by

$$\text{total S wt \%} = \sum_{i=1}^{n} \text{S}(i) \times \text{wt \%}(i) \quad (12)$$

where S(i) is the sulfur wt % in mineral i (including both S in the form of sulfide and sulfate), and wt %(i) is the wt % of mineral i in the sample.

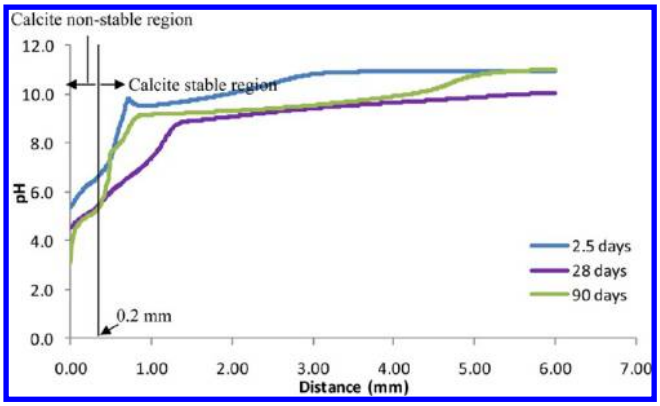

Figure 9. pH changes from the interface region to the interior of the 35:65 sample after 2.5 days, 28 days, and 90 days of exposure.

Compared with the SEM-EDS data, the model simulation results slightly underestimated the S wt% but captured the trend of the change from the interface region to the interior. There were two sulfur-rich zones in samples exposed to CO_2 and H_2S for 28 days. The first zone closer to the brine−cement interface was the zone rich in pyrite, and the zone in the interior was the zone rich in ettringite (Figure 6c). These results were consistent with the experimental results obtained by Kutchko et al.,[7] which showed pyrite formation in the brine-cement interface region and ettringite formation in the interior region of the cement sample.

3.4. Porosity and Permeability. Figure 7 shows predicted spatial distribution of porosity from 2.5 days to 30 years of exposure. Increase in porosity only occurred in the vicinity of the interface (up to 2 mm away from the interface), even when the exposure time was 30 years. The region right next to the interface (Region I in Figure 7) had very high porosity, which was attributed to the dissolution of calcite. The region next to Region I was predicted to have low porosity, which was due to the precipitation of calcite (Region II in Figure 7). The region next to Region II (Region III in Figure 7) was predicted to have high porosity, which was attributed to dissolution of Ca-bearing minerals in this region to produce Ca^{2+}, the source of Ca^{2+} for calcite precipitation in Region II. The porosity of both Region I and Region III increased with the increase of exposure time, contributing to an increase in parallel permeability over time. The porosity of Region II decreased with the increase of exposure time, which contributes to a decrease in transverse permeability over time.

On the basis of the porosity results in Figure 7 and eqs 1−4, the time evolution of the transverse and parallel effective permeability of the whole sample was calculated and results are shown in Figure 8. It can be seen that a rapid increase (several orders of magnitude) in parallel permeability was predicted within 30 days of exposure, followed by much slower increase at longer exposure times.

The calculated transverse effective permeabilities decreased with time. The transverse effective permeability dropped to 0 after 1 year of exposure, due to the formation of the calcite-rich layer. The layer was so dense that it completely blocked the transverse penetration. After 30 years of exposure, the effective parallel permeability of the sample increased by 2.3×10^5 times, while the effective transverse permeability dropped by more than 99%.

This study shows that when the exposure period was relatively short, the formation of ettringite did not have a significant impact

dx.doi.org/10.1021/ef401749x | *Energy Fuels* 2013, 27, 6921−6937

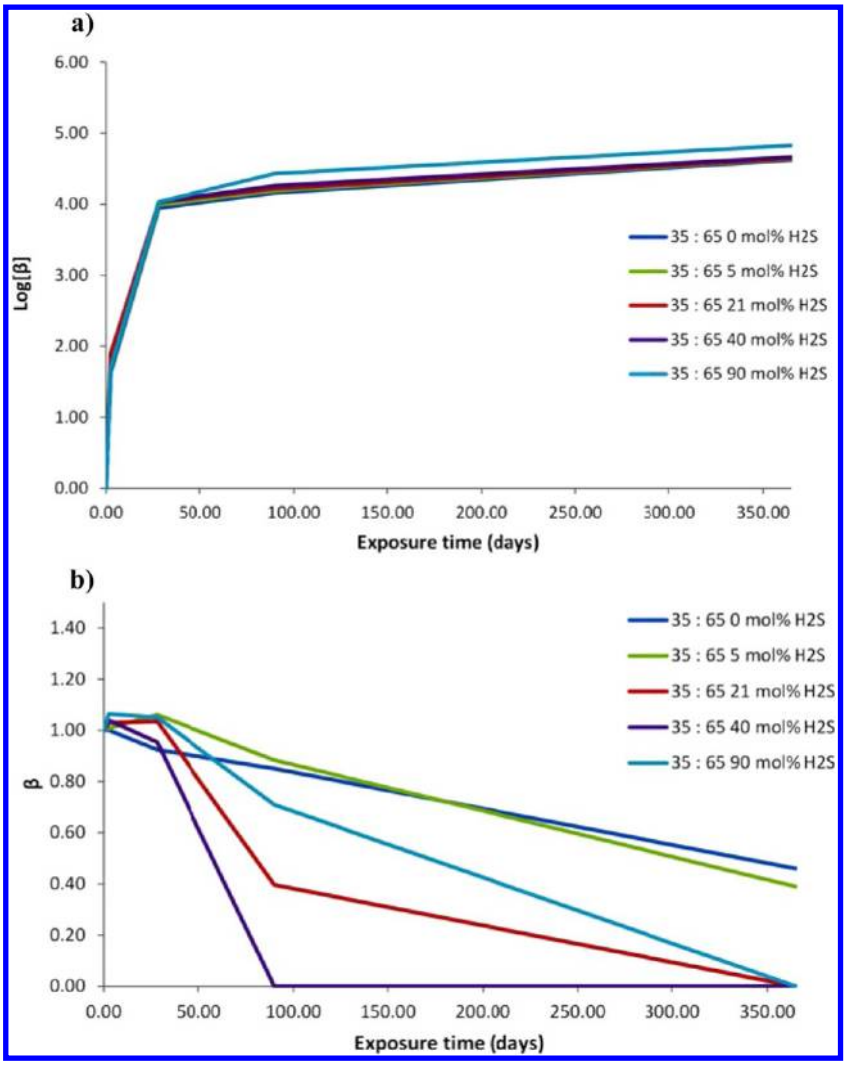

Figure 10. (a) Simulated evolution of effective parallel permeability change as a function of exposure time of the 35:65 sample; (b) simulated evolution of effective transverse permeability change as a function of exposure time of the 35:65 sample.

on porosity of the samples, though ettringite has a very large molar volume compared to many of the cement minerals. For example, when the exposure time was 2.5 days, though ettringite was formed close to the interface of the sample (Figure S-7a, Supporting Information), the porosity of the sample was still high at the interface (Figure 7). However, when the exposure time became long (e.g., 90 days), ettringite precipitation became significant in some regions and the regions with high ettringite content had relatively low porosity. For example, the ettringite content was very high in the region 0.7 mm away from the interface when the exposure time was 90 days (Figure S-7b, Supporting Information), and the porosity of the sample in that region was very low (Figure 7). Therefore, the formation of ettringite has a great effect on porosity of the samples when the exposure time becomes long (90 days or longer).

In neat cement systems, the alteration of cement can lead to the formation of amorphous aluminosilicate phases,[45,50,51] which can reduce the porosity and permeability of cement. However, the formation of amorphous aluminosilicate is not considered in our model, because (1) aluminosilicate phases can react with SO_4^{2-} (from oxidation of H_2S), portlandite and fly ash additives to form ettringite.[51] Therefore, only the modeling of ettringite formation is necessary; (2) the thermodynamic and reaction rate data for amorphous aluminosilicate formation are not available. It is important to note that though aluminosilicate can be converted into ettringite, a precipitation of aluminosilicate can still occur if the conversion rate from aluminosilicate to ettringite is low. As a result, there is a potential for the current model to overestimate the porosity of the samples after exposure to CO_2 and H_2S, because the precipitation of amorphous aluminosilicate is not considered in the model.

3.5. pH. pH is an important parameter that governs mineral dissolution/precipitation reactions in samples exposed to CO_2 and H_2S. Figure 9 shows pH profiles from the interface to the interior of the samples exposed for 2.5, 28, and 90 days. A decrease of pH in the region very close to the interface (0 to 0.2 mm away from the interface) resulted in a dissolution of calcite in this region, as calcite is not stable at low pH (<5 in this study). Beyond that region (>0.2 mm away from the interface), pH is relatively high and calcite is able to precipitate, even after a long time of exposure. The pH results also show that due to the diffusion of CO_2 and H_2S to the interior region, there was a pH drop throughout the entire sample from 2.5 days of exposure to 28 days of exposure. However, due to both the blockage of CO_2 and H_2S to the interior by the calcium carbonate layer and equilibrium with the fluid in a batch system, the pH in the interior

dx.doi.org/10.1021/ef401749x | *Energy Fuels* 2013, 27, 6921−6937

region (>0.2 mm away from the interface) increased from 28 days of exposure to 90 days of exposure. The increase of pH in the interior region would suppress the dissolution of cement minerals and the increase of porosity in the interior region. The pH results explain why after 90 days, the porosity increase in the interior region was significantly slowed down.

3.6. Effect of H_2S Content in Acid Gas on Permeability Change. The effect of H_2S content in acid gas on permeability of wellbore cement was studied with the model. Figure 10 shows the simulated evolution of parallel and transverse effective permeability from 0 to 1 year of exposure, for different H_2S mol %. The change in H_2S mol % did not have a significant effect on parallel effective permeability change in the exposure time range of 0 to 1 year. As to transverse effective permeability, the increase of H_2S mol % resulted in a simulated decrease of transverse effective permeability, which was attributed to an enhanced precipitation of $CaCO_3$ with continuous dissolution of Ca-bearing minerals in the interior region. Compared with CO_2, H_2S has a higher solubility in brine and penetrates faster in cement, and thus an increase in H_2S content in CO_2 and H_2S mixture results in faster pH drop in the interior region of the cement, and more Ca-bearing minerals in the interior region get dissolved. The enhanced dissolution of Ca-bearing minerals provided more Ca^{2+} to form a denser calcite-rich layer, which reduced transverse effective permeability. However, when the H_2S content is very high (e.g., 90 mol % H_2S in CO_2 and H_2S mixture), there is not enough carbonate species in the brine to form $CaCO_3$, and thus the $CaCO_3$-rich layer becomes porous. Please refer to Figure S-8 in Supporting Information for details.

4. CONCLUSIONS

A reactive transport model that can simulate the interactions between pozzolan-amended wellbore cement and acid gas (CO_2 + H_2S) under geologic carbon sequestration conditions was developed by using the reactive transport code CrunchFlow. Given the initial composition of pozzolan-amended wellbore cement, pressure, temperature, and composition of acid gas (e.g., mol % of H_2S and CO_2), the model was able to accurately predict the experimental observation of the calcite volume percentage, total Ca weight percentage, and total S weight percentage, and the evolution of porosity and effective permeability over time.

The simulation results (calcite vol %, total Ca wt % and total S wt %) were able to describe the experimental data with adjustment of chemical reaction rate constants and in some cases tortuosity values. The model predicted the formation of a narrow calcite layer (about 0.2 mm thick) in the interface region of the sample after 2.5 days of exposure, and the layer became dense (peak calcite vol% in the layer reached 55%) after 90 days of exposure. C−S−H was the primary Ca^{2+} source to form the calcite layer, followed by C3S and $Ca(OH)_2$. The main products of interaction between the 35:65 sample and H_2S were pyrite and ettringite. Pyrite was mainly formed in the region between interface and 0.5 mm away from interface. Ettringite was mainly formed within 1 mm distance from the interface. Because of redissolution of calcite in the region close to the interface, there was a significant increase in effective parallel permeability of the sample after 2.5 days of exposure. After 1 year of exposure, the effective transverse permeability decreased by more than 99%.

When H_2S content in the CO_2−H_2S supercritical mixture is in the range of 0 mol % to 40 mol % (a 40 mol % H_2S in CO_2−H_2S supercritical mixture corresponds to 1.73 mol/L H_2S and 0.87 mol/L CO_2 in brine, given a supercritical mixture pressure of 150 bar), an increase in H_2S content results in more dissolution of Ca-bearing minerals in cement due to fast penetration of H_2S to the interior and subsequent pH decrease in the interior, which also leads to more precipitation of calcite. Those effects contribute to a negligible change in parallel permeability and a decrease in transverse permeability. When H_2S content in the supercritical CO_2 and H_2S mixture is very high (e.g., 90 mol %, corresponding to 2.40 mol/L H_2S and 0.28 mol/L CO_2 in brine, given a supercritical mixture pressure of 150 bar), calcite precipitation rate is reduced due to the lack of carbonate species, and the calcite-rich layer forms slower than cases with higher CO_2 content. Those effects contribute to an increase in parallel permeability. As to transverse permeability, the precipitation of calcite is still enough to reduce the permeability to nearly 0 after 1 year of exposure to 90 mol % H_2S.

Although the simulation results in this work are about pozzolan-amended wellbore cement exposed to brine saturated with a mixture of CO_2−H_2S, the results show similar characteristics with those for neat cement samples under similar exposure conditions.[7,8] Kutchko et al.[7] observed the formation of calcite close to the interface of cement and partial dissolution of calcite in contact with brine saturated with CO_2 and H_2S. Kutchko et al. also observed the formation of pyrite in the carbonated interface region of the cement and the formation of ettringite in the interior region. All the observations are consistent with the simulation results in this work. For porosity, both experimental observations and model simulation results[8] show a thin layer with low porosity close to the interface of cement (due to calcite precipitation) and a layer with much higher porosity next to the low-porosity layer (due to dissolution of various Ca-bearing minerals in this layer), which are consistent with porosity results from this work.

Overall, this research indicates that the interaction between pozzolan-amended cement and CO_2 mainly results in dissolution of Ca-bearing minerals (C−S−H, C3S, $Ca(OH)_2$, etc) and precipitation of calcite. The interaction between pozzolan-amended cement and H_2S mainly results in the formation of pyrite and ettringite. In short exposure time (<90 days), it is the dissolution of Ca-bearing minerals and the precipitation of calcite that govern porosity and permeability evolution. When the exposure time becomes long (>90 days), the formation of ettringite also contributes to porosity and permeability evolution. The formation of a highly porous zone at the surface of the sample in contact with brine saturated with CO_2 and H_2S contributes to 5 orders of magnitude increase in effective parallel permeability after 30 years of exposure. If there is microannulus between cement and formation, the leakage risk can become significant, because the microannulus would be in full contact with the brine and a large increase in parallel permeability can result in fast leakage. However, if cement and formation are bonded well and there is no microannulus between cement and formation, the increase in effective parallel permeability does not result in potential for leakage, because only the bottom portion of the wellbore contacts the brine. The other portions of the well would not directly contact the brine. Therefore, more investigations are needed to correlate the effective permeability change of the wellbore cement in contact with brine and the effective permeability change of the wellbore cement of the entire cemented well.

dx.doi.org/10.1021/ef401749x | Energy Fuels 2013, 27, 6921−6937

■ ASSOCIATED CONTENT

Supporting Information

Literature sources of equilibrium constants and rate constants for all reactions involved in the reactive transport modeling, optimization of reaction rate constants, validation of model outputs by SEM-EDS data, and simulated CO_2 and H_2S concentrations in exposed samples. This information is available free of charge via the Internet at http://pubs.acs.org/.

■ AUTHOR INFORMATION

Corresponding Author

*E-mail: zlwe88@gmail.com.

Notes

Disclaimer: The views and opinions of authors expressed herein do not necessarily state or reflect those of the United States Government or any agency thereof.

The authors declare no competing financial interest.

■ ACKNOWLEDGMENTS

This work was supported by the Carbon Sequestration Program of the U.S. DOE National Energy Technology Laboratory (NETL) and U.S. DOE National Energy Technology Laboratory—Regional University Alliance (RUA) Partnership, under Contract Number RES1000025. The authors appreciate the support of laboratory work conducted at the University of North Dakota Environmental and Energy Research Center under the Plains CO_2 Reduction Partnership (PCOR), which is supported by NETL. The authors also thank Ron Ripper of Civil and Environmental Engineering Lab, and Tom Nuhfer and Jason Wolf at Material Science and Engineering at CMU for assistance with laboratory instrumentation. The authors would also like to thank Barbara Kutchko, Christina Lopano, and Brian Strazisar at NETL for their invaluable comments on this paper.

■ REFERENCES

(1) Houghton, J. T.; Ding, Y.; Griggs, D. J.; Noguer, M.; van der Linden, P. J.; Xiaosu, D., Eds.; Cambridge University Press, New York, 2001.

(2) Gasda, S. E.; Bachu, S.; Celia, M. A. *Environ. Geol.* **2004**, *46* (6−7), 707−720.

(3) *IPCC (Intergovernmental Panel on Climate Change), Fourth Assessment Report*, IPCC Secretariat: Geneva, Switzerland, 2007.

(4) Global CCS Institute: Canberra, Australia, 2011.

(5) Jacquemet, N.; Pironon, J.; Saint-Marc, J. *Environ. Sci. Technol.* **2008**, *42* (1), 282−288.

(6) Hawthorne, S. B.; Miller, D. J.; Holubnyak, Y.; Harju, J. A.; Kutchko, B. G.; Strazisar, B. R. *Energy Procedia* **2011**, *4*, 5259−5266.

(7) Kutchko, B. G.; Strazisar, B. R.; Hawthorne, S. B.; Lopano, C. L.; Miller, D. J.; Hakala, J. A.; Guthrie, G. D. *Int. J. Greenhouse Gas Con.* **2011**, *5* (4), 880−888.

(8) Jacquemet, N.; Pironon, J.; Lagneau, V.; Saint-Marc, J. *Appl. Geochem.* **2012**, *27*, 782−795.

(9) Bachu, S.; Adams, J. J.; Michael, K.; Buschkuehle, B. E. In *Proceedings of the Second Annual Conference on Carbon Dioxide Sequestration*; Alexandria, VA, 2003.

(10) Benson, S. M.; Apps, J.; Hepple, R.; Lippmann, M.; Tsang, C. F.; Lewis, C. In *GHGT-6: Sixth International Conference on Greenhouse Gas Control Technologies*; Kyoto, Japan, 2003

(11) Keating, E. H.; Newell, D. L.; Viswanathan, H.; Carey, J. W.; Zyvoloski, G.; Pawar, R. *Environ. Sci. Technol.* **2013**, *47*, 290−297.

(12) Nordbotten, J. M.; Celia, M. A.; Bachu, S.; Dahle, H. K. *Environ. Sci. Technol.* **2005**, *39*, 602−611.

(13) Apps, J. A.; Zheng, L.; Zhang, Y.; Xu, T.; Birkholzer, J. T. *Transport Porous Med.* **2010**, *82*, 215−246.

(14) Battani, A.; Deville, E.; Faure, J. L.; Jeandel, E.; Noirez, S.; Tocque, E.; Benoit, Y.; Schmitz, J.; Parlouar, D.; Sarda, P.; Gal, F.; Le Pierres, K.; Brach, M.; Braibant, G.; Beny, C.; Pokryszka, Z.; Charmoille, A.; Bentivegna, G.; Pironon, J.; de Donato, P.; Garnier, C.; Cailteau, C.; Barres, O.; Radilla, G.; Bauer, A. *Oil Gas Sci. Technol.* **2010**, *65*, 615−633.

(15) Carroll, S.; Hao, Y.; Aines, R. *Geochem. Trans.* **2009**, *10* (4), 1−18.

(16) Frye, E.; Bao, C.; Li, L.; Blumsack, S. *Environ. Sci. Technol.* **2012**, *46*, 4388−4395.

(17) Theresa, L.; Watson, T. L.; Bachu, S. *SPE Drill. Completion* **2009**, *24* (1), 115−126.

(18) Zhang, L.; Dzombak, D. A.; Nakles, D. V.; Hawthorne, S. B.; Miller, D. J.; Kutchko, B. G.; Lopano, C. L.; Strazisar, B. R. *Int. J. Greenhouse Gas Control* **2013**, *19*, 358−368.

(19) Malhotra, V. M.; Mehta, P. K. *Pozzolanic and Cementitious Materials*; Overseas Publisher Association: Amsterdam, 1996.

(20) Ghosh, S. N. *Cement and Concrete Science and Technology*; ABI Books Private Limited: New Dehli, 1991.

(21) *API Spec 10A: Specification for Cements and Materials for Well Cementing*, 21st ed.; API: Washington, DC, 1991.

(22) Huet, B. M.; Prevost, J. H.; Scherer, G. W. *Int. J. Greenhouse Gas Control* **2010**, *4*, 561−574.

(23) Gherardi, F.; Audigane, P.; Gaucher, E. C. *J. Hydrol.* **2012**, *420−421*, 340−359.

(24) Brunet, J. L.; Li, L.; Karpyn, Z. T.; Kutchko, B. G.; Strazisar, B. R.; Bromhal, G. *Energy Fuels* **2013**, *27* (8), 4208−4220.

(25) Ghabezloo, S.; Sulem, J.; Saint-Marc, J. *Int. J. Rock Mech. Min.* **2009**, *46* (4), 761−768.

(26) Bernabe, Y.; Mok, U.; Evans, B. *Pure Appl. Geophys.* **2003**, *160* (5), 937−960.

(27) Luquot, L.; Gouze, P. *Chem. Geol.* **2009**, *265* (1−2), 148−159.

(28) McCune, C. C.; Fogler, H. S.; Kline, W. E. *Ind. Eng. Chem. Fund.* **1979**, *18* (2), 188−191.

(29) Noiriel, C.; Bernard, D.; Gouze, P.; Thibault, X. *Oil Gas Sci. Technol. − Rev. IFP* **2005**, *60* (1), 177−192.

(30) Noiriel, C.; Gouze, P.; Bernard, D. *Geophys. Res. Lett.* **2004**, *31* (24), L24603.

(31) Craft, B. C.; Hawkins, M. F.; Terry, R. E. *Applied Petroleum Reservoir Engineering* ; Prentice Hall: Englewood Cliffs, NJ, 1991; p 431.

(32) Steefel, C. I. *CrunchFlow User's Manual*; Lawrence Berkeley National Laboratory: Berkeley, CA, 2009.

(33) Steefel, C. I.; Maher, K. *Rev. Mineral. Geochem.* **2009**, *70* (1), 485−532.

(34) Li, L.; Steefel, C. I.; Kowalsky, M. B.; Englert, A.; Hubbard, S. S. *J. Contam. Hydrol.* **2010**, *112*, 45−63.

(35) Li, L.; Gawande, N.; Kowalsky, M. B.; Steefel, C. I.; Hubbard, S. S. *Environ. Sci. Technol.* **2011**, *45*, 9959−9966.

(36) *API Recommended Practice 10B: Recommended Practice for Testing Well Cements*; API: Washington, DC, 1997.

(37) Steefel, C. I.; Lasaga, A. C. *Am. J. Sci.* **1994**, *294* (5), 529−592.

(38) Xu, T.; Sonnenthal, E.; Spycher, N.; Pruess, K. Paper LBNL-55460; Lawrence Berkeley National Laboratory: Berkeley, CA, 2004.

(39) Marty, N. C. M.; Tournassat, C.; Burnol, A.; Giffaut, E.; Gaucher, E. C. *J. Hydrol.* **2009**, *364* (1−2), 58−72.

(40) Wilke, C. R.; Chang, P. *AIChE J.* **1955**, *1* (2), 264−270.

(41) Promentilla, M. A. B.; Sugiyama, T.; Hitomi, T.; Takeda, N. *Cem. Concr. Res.* **2009**, *39* (6), 548−557.

(42) Arnold, J.; Meeussen, J.; Garrabrants, A.; van der Sloot, H. A.; Kosson, D. S. WM symposia, Phoenix, AZ, 2010.

(43) Duguid, A.; Radonjic, M.; Scherer, G. Fourth Annual Conference on Carbon Capture and Sequestration, Pittsburgh, PA, 2005.

(44) Walsh, S. D.; Du Frane, W. L.; Mason, H. E.; Carroll, S. A. *Rock Mech. Rock Eng.* **2013**, *46* (3), 455−464.

(45) Mason, H. E.; Du Frane, W. L.; Walsh, S. D.; Dai, Z.; Charnvanichborikarn, S.; Carroll, S. A. *Environ. Sci. Technol.* **2013**, *47* (3), 1745−1752.

(46) Kutchko, B. G.; Strazisar, B. R.; Dzombak, D. A.; Lowry, G. V.; Thaulow, N. *Environ. Sci. Technol.* **2007**, *41* (13), 4787−4792.

(47) Carey, J. W.; Svec, R.; Grigg, R.; Zhang, J.; Crow, W. *Int. J. Greenhousw Gas Control* **2010**, *4*, 272−282.

(48) Barlet-Gouédard, V.; Rimmelé, G.; Goffé, B.; Porcherie, O. *Oil Gas Sci. Technol.* **2007**, *62*, 325−334.
(49) Fabbri, A.; Corvisier, J.; Schnubel, A.; Brunet, F.; Goffé, B.; Rimmelé, G.; Barlet-Gouédard, V. *Cem. Concr. Res.* **2009**, *39*, 1156−1163.
(50) Brown, P. W.; Doerr, A. *Cem. Concr. Res.* **2000**, *30*, 411−418.
(51) Scherer, G. W.; Kutchko, B. G.; Thaulow, N.; Duguid, A.; Mook, B. *Int. J. Greenhouse Gas Control* **2011**, *5* (1), 115−124.
(52) Duan, Z. H.; Sun, R. *Chem. Geol.* **2003**, *193*, 257−271.
(53) Duan, Z. H.; Sun, R.; Liu, R.; Zhu, C. *Energy Fuels* **2007**, *21*, 2056−2065.
(54) Glasser, F. P. *J. Hazard. Mater.* **1997**, *52* (2−3), 151−170.
(55) Lothenbach, B.; Matschei, T.; Möschner, G.; Glasser, F. P. *Cem. Concr. Res.* **2008**, *38* (1), 1−18.
(56) Abo-El-Enein, S. A.; Goto, S.; Kondo, R.; Mikhail, R. S. *J. Appl. Chem. Biotechnol.* **1977**, *27* (1), 375−381.
(57) Lee, J. H. Ph.D. dissertation, University of Michigan, 2009; p 17
(58) Dzombak, D. A.; Morel, F. M. M. *Surface Complexation Modeling: Hydrous Ferric Oxide*; John Wiley & Sons, Inc., Hoboken, NJ, 1990.
(59) Cussler, E. L. *Diffusion: Mass Transfer in Fluid Systems* ; Cambridge University Press: Cambridge, UK, 2009.
(60) Price, W. E.; Woolf, L. A. *J. Solution Chem.* **1992**, *21* (3), 239−248.
(61) Reiners, G.; Lorenz, W. J.; Hertz, H. G. *Berich. Bunsen. Gesell.* **1978**, *82* (7), 738−744.
(62) Landolt, D. *Corrosion and Surface Chemistry of Metals*; CRC Press, Taylor & Francis Group LLC: Boca Raton, FL, 2007.
(63) Lide, D. R., Eds. *CRC Handbook of Chemistry and Physics*, 89th ed.; CRC Press, Taylor & Francis Group LLC: Boca Raton, FL, 2009.